Synthesis and characterization of plasmonic Au/TiO$_2$ nanorod solids for heterogeneous photocatalysis

Špela Slapničar [a], Gregor Žerjav [a], Janez Zavašnik [b], Matjaž Finšgar [c], Albin Pintar [a,*]

[a] *Department of Inorganic Chemistry and Technology, National Institute of Chemistry, Hajdrihova 19, SI-1001 Ljubljana, Slovenia*
[b] *Gaseous Electronics, Jožef Stefan Institute, Jamova 39, SI-1000 Ljubljana, Slovenia*
[c] *University of Maribor, Faculty of Chemistry and Chemical Engineering, Smetanova 17, SI-2000 Maribor, Slovenia*

ARTICLE INFO

ABSTRACT

Plasmonic Au (1 wt%) catalysts deposited on hydrothermally synthesized TiO$_2$ nanorods (TNR) were investigated in this study. Based on the duration of mixing of the Au precursor/TNR suspension during the wet impregnation synthesis and parameters of the end calcination, Au/TiO$_2$ catalysts with different sizes of Au nanoparticles (Au NPs) were obtained. The prepared solids were thoroughly characterized by several instrumental techniques to investigate property-activity relationships. Regardless of the size of Au particles on the catalyst surface, an absorption peak at 550 nm occurred in all UV-Vis diffuse reflectance spectra of the investigated Au/TiO$_2$ catalysts, which is characteristic of the localized surface plasmon resonance effect exerted by metallic Au NPs. By measuring the formation of reactive oxygen species under visible-light illumination using various scavengers, the production of superoxide anion radicals (O$_2^{\bullet-}$) and hydroxyl radicals were identified, however, the former were found to represent the main reactive oxygen species that govern the oxidation of aqueous bisphenol A (BPA) employed as a model organic pollutant. The activity of Au/TiO$_2$ catalysts for the generation of O$_2^{\bullet-}$ radicals (and BPA oxidation) increases by increasing the Schottky barrier height, which is due to the slow reduction of water-dissolved O$_2$ on the catalyst surface.

1. Introduction

In recent decades, developing techniques for environmentally friendly wastewater treatment has become of significant importance. Many efforts have been made to develop advanced oxidation processes (AOPs) that would efficiently remove persistent water-dissolved organic pollutants [1]. Besides, the developed purification techniques need to be ecological and economical.

Heterogeneous photocatalysis is representative of AOPs, where a catalyst is illuminated with light to trigger a heterogeneously catalyzed reaction. We are focused on a semiconducting photocatalyst, i.e. titanium dioxide (TiO$_2$) [1–4]. Semiconductors have a valence band (VB), a conduction band (CB), and an interim band gap (BG). Electrons are transferred from the VB to the CB upon excitation, creating $e^- $-$h^+$ pairs. Charge carriers on the surface of a photocatalyst can subsequently participate in redox reactions (e.g. generation of reactive oxygen species). In reaction with water-dissolved oxygen (O$_2$), there is a reduction of O$_2$ to superoxide anion radicals (O$_2^{\bullet-}$); the latter are involved in subsequent liquid-phase reactions to produce hydroxyl radicals (OH$^\bullet$)

[4]. Also, we know two types of oxidation reactions: direct and indirect. Direct oxidation occurs on the surface of the semiconductor, where adsorbed organic molecules react with a VB hole (h^+). On the other hand, indirect oxidation occurs when OH$^\bullet$ is formed after a reaction of water molecule adsorbed on the catalyst surface (or surface hydroxyl group) and h^+, and then OH$^\bullet$ reacts with an organic molecule [5].

The semiconductor TiO$_2$ is known for high photocatalytic activity [6], stability in water, low cost, and low toxicity [7–10]. Due to these advantages, TiO$_2$ is one of the best semiconducting oxides and a versatile material for heterogeneous photocatalysis. Its disadvantage is a wide band gap (3.2 eV for anatase TiO$_2$) [8,9,11,12,13], which means that it could only be activated by UV-light illumination. In the solar light spectrum, there is only 3–4% of UV light [12,14]. However, this drawback could be, for instance, overcome by depositing nanoparticles (NPs) of a plasmonic metal (e.g. Au) on the surface of TiO$_2$, which in turn would allow harvesting of visible light and near-infrared radiation of the solar spectrum. Kumar et al. [15] studied the influence of different crystalline phases of TiO$_2$ (amorphous, anatase, and rutile) on the properties of Au/TiO$_2$ catalysts. The deposition of gold nanoparticles

* Corresponding author.
  E-mail address: albin.pintar@ki.si (A. Pintar).

was carried out using the sol-gel method, with gold particles synthesized using the seed-growth method. They studied the activity of the catalysts by degradation of different types of benzyl alcohols. Formed Au nanoparticles have unique optical and electronic properties [14]. For instance, Singh et al. [16] investigated the optical properties of Au/TiO$_2$ catalysts by varying the TiO$_2$ crystal structure (anatase and rutile) and observed that the addition of Au nanoparticles to the support significantly increased the optical absorption capacity; the enhanced absorption in the visible region was attributed to the surface plasmon resonance (SPR) effect of gold nanoparticles. Gold nanoparticles were synthesized using different concentrations of sodium citrate. The photocatalytic activity of the prepared Au/TiO$_2$ catalysts was investigated under sunlight illumination, which means that the catalytic activity of TiO$_2$ was also triggered. Au/TiO$_2$ catalysts, especially when TiO$_2$ is present in the form of nanorods, exhibit a strong visible-light absorption band occurring as a hump at 500–600 nm due to the localized SPR effect [13,17]. SPR effect leads to the formation of "hot electrons", which are injected from Au nanoparticles into the CB of TiO$_2$. Furthermore, at the interface between the Au and TiO$_2$ phases, a so-called Schottky barrier (SB) is formed. The height of the Schottky barrier (SBH) is an important parameter that affects the mobility of the plasmon-induced "hot electrons" at the plasmonic metal/semiconductor interface [18]. The presence of SB significantly inhibits the recombination of "hot electrons" by facilitating their separation and utilization in redox processes, which plays a key role in photocatalytic reactions and photovoltaic devices [19–21]. An in-depth understanding of the effect of SBH on plasmonic metal/TiO$_2$ is crucial since the photocatalytic activity of catalysts containing plasmonic metals is influenced by the transfer of "hot electrons" from the plasmonic metal to the conduction band of the TiO$_2$ semiconductor [22].

Gold nanoparticles are known for their stability, non-toxicity, and biocompatibility [23]. They are generally active under mild conditions (e.g. ambient temperature), which makes them unique, according to Thompson [24]. Gold nanoparticles are known for various applications, for example in medicine as drug delivery agents [25] and in the diagnosis of diseases [26] (cancer, heart disease); they are also used as various types of sensors [27] and as catalysts [28] in chemical reactions. The size of Au nanoparticles is important in any catalytic process and depends on the utilized stirring times and calcination during the catalyst preparation procedure [29]. Deposition of smaller nanoparticles on a catalyst support results in more uniform dispersion over the TiO$_2$ surface [30]. Some studies showed that smaller Au particles are more active compared to larger Au nanoparticles [31,32]. However, Yoo et al. [33] showed that the LSPR effect occurs in larger gold nanoparticles, which is crucial in prolonging the lifetime of charge carriers, leading to better photocatalytic activity. The performance of Au/TiO$_2$ catalysts is a complicated interplay between the size of Au nanoparticles, their separation, etc.

The present work aimed to study in detail the morphological, surface, optical, and electronic properties of Au/TiO$_2$ nanorod catalysts (prepared by a wet impregnation synthesis applying different preparation protocols) using various characterization techniques, and to verify the ability of the investigated Au/TiO$_2$ catalysts to generate charge carriers and reactive oxygen species (ROS) under visible-light illumination. In addition, the visible-light-triggered activity and performance of the synthesized Au/TiO$_2$ catalysts were tested in the reaction of heterogeneous photocatalytic degradation of water-dissolved model organic pollutant bisphenol A (BPA). Utilization of the obtained results enabled us to systematically compare the influence of the catalyst synthesis conditions (i) on the particle size of formed Au ensembles, (ii) on the properties of Au/TiO$_2$ catalysts, and (iii) photocatalytic activity.

2. Experimental

2.1. Materials

Sodium hydroxide (NaOH, ≥98%, Merck), hydrochloric acid (HCl, fuming 37%, ≤1 ppm free chlorine, Merck), gold (III) chloride hydrate (HAuCl$_4$·xH$_2$O, ~50% Au basis, Sigma Aldrich), absolute ethanol (C$_2$H$_5$OH, ≥99.5%, Carlo Erba reagents), coumarin (COUM, ≥98%, Thermo Fisher), 1,1-diphenyl-2-picrylhydrazyl (DPPH, Sigma Aldrich), 2,2′-azino-bis-(3-ethylbenzothiazoline-6-sulfonic acid) cation (ABTS$^{•+}$, ≥98%, Sigma Aldrich), potassium persulfate (K$_2$S$_2$O$_8$, ≥99%, Sigma Aldrich), α-(4-Pyridyl 1-oxide)-N-tert-butylnitrone (POBN, ≥99%, Sigma Aldrich), hydrogen peroxide solution (H$_2$O$_2$, 30% (m/m) in water, Merck) and bisphenol A (BPA, ≥99%, Sigma Aldrich) were used as received. TiO$_2$ precursor DT-51 was donated from the company CristalACTiV™. All aqueous solutions used in this work were prepared with ultrapure water (18.2 MΩ cm) and kept in the dark at 4 °C.

2.2. Catalyst synthesis

Titanate nanorods (TNR) were prepared by hydrothermal synthesis [13,34]. For this purpose, 2 g of TiO$_2$ precursor (DT-51, CristalACTiV™) was dispersed in an aqueous sodium hydroxide solution (10 M). The suspension was heated at 130 °C for 24 h in a Teflon-lined autoclave. After 24 h, the obtained precipitate was separated by centrifugation and washed several times thoroughly with 0.1 M HCl and ultrapure water. The obtained material (TNR) was calcined at 500 °C for 2 h in air with a heating ramp of 120 °C per hour.

A wet impregnation technique was used to deposit nanoparticles (NPs) of Au on TNR. The preparation procedure was similar to the one used by Verma et al. [35]. The TNR support was dispersed in ethanol or pure water by ultrasonication for 10 min, and then Au precursor (HAuCl$_4$) was added in the amount that resulted in the metal loading of 1.0 wt%. Afterward, the suspension was continuously stirred for either 2 h or 21 h. The solvent was then evaporated using a rotary evaporator, and the obtained material was dried at 80 °C for 18 h. Further, the sample was calcined at 300 °C for 2 h in a 5% H$_2$/95% N$_2$ gas mixture with a heating ramp of 150 °C per hour [35]. We prepared four different Au/TiO$_2$ catalysts and optimized the synthesis of the most photocatalytically active catalyst with different synthesis parameters (solvent, stirring time, and calcination temperature): (i) TNR dispersed in ethanol, stirred for 2 h and calcined as described above (denoted as NP1), (ii) TNR dispersed in ethanol and stirred for 2 h, not calcined (denoted as NP2), (iii) TNR dispersed in ethanol, stirred for 21 h and calcined (denoted as NP3), and (iv) TNR dispersed in water and stirred for 2 h and calcined (denoted as NP4).

2.3. Catalyst characterization

UV-Vis diffuse reflectance (UV-Vis DR) spectra of the investigated catalysts were measured in the wavelength range between 200 and 900 nm at room temperature and a scan rate of 266.75 nm per minute, using a UV-Vis spectrophotometer (Perkin Elmer, model Lambda 650), equipped with a Praying Mantis, DRP-SAP accessory from Harrick. A Perkin Elmer UV-Vis fluorescence spectrometer LS 55 was used to measure the photoluminescence (PL) of solid samples. The excitation wavelength was 300 nm, the excitation slit 5 nm, the emission slit 7.5 nm, and the scan speed was set to 200 nm per minute. The wavelength range was adjusted from 300 to 600 nm.

A transmission electron microscope (TEM, JEM-2100, JEOL Inc.) and scanning electron microscope (SEM, SUPRA 35 VP, Carl Zeiss) equipped with energy-dispersive X-ray spectrometer (SEM-EDXS, Inca 400, Oxford Instruments) were used to analyze the morphology and chemical composition of the investigated materials. For TEM analysis, the samples were diluted in ethanol, sonicated for 30 s in an ultrasonic bath, and dip-transferred on commercial amorphous carbon support grids. For the

SEM-EDXS analysis, the powdered catalysts were attached to an aluminum holder with double side carbon tape and afterward purged by a stream of nitrogen to remove the residual amount of samples that were not attached to the carbon tape.

N_2 physisorption measurements were performed by employing a Micromeritics TriStar II 3020 analyzer. Before measurements, the catalysts were degassed with N_2 (purity 6.0) in a Micromeritics' SmartPrep unit at 90 °C for 60 min and 180 °C for 240 min for calcined samples, and at 80 °C for 1260 min for the non-calcined sample. The specific surface area was calculated using the Brunauer-Emmett-Teller (BET) method, while the Barrett-Joyner-Halenda (BJH) method was used to calculate the total pore volume and pore size distribution from desorption isotherms.

Temperature-programmed reduction (H_2-TPR) measurements were performed using an AutoChem II 2920 analyzer from Micromeritics, equipped with a Thermal Conductivity Detector (TCD). During the H_2-TPR measurement, 80 mg of a catalyst sample was positioned on a quartz wool flock inside a U-shaped quartz tube and pretreated in 5% O_2/He stream (25 mL per minute) at 300 °C for 10 min. This step was followed by cooling the sample to 50 °C. After 10 min of purging in Ar flow (25 mL per minute), the gas flow was switched to 5% H_2/Ar (25 mL per minute), and a linear temperature ramp of 10 °C per hour was employed until the final temperature of 800 °C was reached. A liquid isopropanol/LN_2 cold trap ($T \approx -80$ °C) was used to condense water and eliminate its contribution to the recorded H_2-TPR profiles.

Crystallinity and phase composition of the synthesized catalysts were analyzed by powder X-ray diffraction (XRD) using a PANalytical X′Pert Pro diffractometer with Cu $K_{\alpha 1}$ radiation ($\lambda = 0.15406$ nm). The catalysts were scanned in the 2θ range between 5° and 90°, with step increments of 0.033° and 100 s step time.

The photoresponse characteristics (photocurrent density measurements) of the investigated materials under visible-light illumination (Schott, model KL 2500 LED) were evaluated using a Metrohm Autolab PGSTAT30 potentiostat/galvanostat and a three-electrode electrochemical cell. A 0.1 M KOH aqueous solution was used as an electrolyte. A screen-printed electrode (DropSens, model DRP-150) was used as the working electrode in the present electrochemical experiment. On the working electrode, a 10 μL drop of catalyst-ethanol suspension (10 mg of catalyst in 0.5 mL of absolute ethanol (Sigma Aldrich)) was applied and left to dry. The counter electrode was a platinum sheet (Metrohm, model 3.109.0790), and the calomel electrode HI5412 (HANNA instruments) served as the reference electrode. The same setup was used to perform the electrochemical impedance spectroscopy (EIS) measurements in the frequency range 10^{-1}-10^6 Hz.

X-ray photoelectron spectroscopy (XPS) measurements were performed using a Supra+ device (Kratos, Manchester, UK) with an Al K_α excitation source. Powder samples were attached to the carbon tape on the Si wafer. During the measurements, a charge neutralizer was on. Spectra acquisition was carried out at a pass energy of 20 eV and a take-off angle of 90°. The binding energy of the spectra was corrected using a C-C/C-H peak in the C 1 s spectrum positioned at 284.8 eV. Spectra acquisition and processing were performed using ESCApe 1.5 software (Kratos).

Continuous wave X-band electron paramagnetic resonance (EPR) experiments were performed using a bench-top EPR spectrometer (Adani, model CMS 8400) operating at a microwave frequency of 9.4 GHz. The EPR spectra were recorded with a modulation amplitude of 100 μT and a modulation frequency of 10 dB. The microwave power was 9 mW. A liquid-phase reaction of POBN with OH• radicals was set in a 100 mL batch reactor made of glass. The aqueous suspension of NP1 catalyst and POBN was first stirred in the dark for 30 min, and then the visible-light illumination (Schott, model KL 2500 LED) was switched on. We collected aqueous-phase samples every hour, transferred them into a thin-walled quartz tube (Wilmad, model WG-808-Q), and acquired the EPR spectra of POBN-OH adduct to follow the formation of OH• radicals [36].

2.4. Evaluation of the photocatalytic activity

For measuring the light-triggered generation of different ROS, we prepared (i) a 200 mg/L aqueous solution of coumarin (COUM) to follow the formation rate of OH• radicals under visible-light illumination by producing 7-hydroxycoumarin (7-OHC) [17,37], (ii) a 40 μM solution of (2,2-diphenyl-1-picrylhydrazyl) (DPPH) in water:ethanol mixture (1:1, v/v) to follow the generation of electrons, holes, OH• and $O_2^{\bullet -}$ [38–41], and (iii) an aqueous solution of ABTS•+, where we dissolved 17.2 mg of 2,2′-azino-bis(3-ethylbenzothiazoline-6-sulphonic acid) salt (ABTS•+) and 3.3 mg of $K_2S_2O_8$ in 5 mL of ultrapure water to follow the formation of electrons and $O_2^{\bullet -}$ [40].

We performed the reaction using COUM by adding 10 mg of the prepared catalysts into 50 mL of the COUM solution, which was stirred at 400 rpm in a 100 mL batch reactor made of glass. The suspension was first stirred in the dark for 20 min to establish the sorption equilibrium. Then, the visible-light source (Schott, model KL 2500 LED) was switched on, and liquid-phase samples were collected at defined time intervals and filtered through a 0.2 μm membrane filter. Afterward, the samples were measured on the UV-Vis photoluminescence spectrometer (Perkin Elmer, model LS 55) using a 10 × 10 mm quartz cuvette. The excitation wavelength was set to 338 nm, the excitation and emission slits to 10 nm, and the scan speed to 200 nm per minute. The photoluminescence intensity of 7-OHC produced was measured at $\lambda = 456$ nm [37]. The experimental set-up and operating conditions for the measurements with DPPH and ABTS•+ (1 mL of ABTS•+ solution diluted in 50 mL of ultrapure water) followed the same experimental set-up and the protocol as in the case of COUM measurements, with the only difference that 1 mg of the catalyst sample was used in the case of DPPH. The temporal concentration of DPPH was measured by acquiring UV-Vis spectra (Perkin Elmer, model Lambda 465) using a quartz cuvette with a 10 mm optical path; for quantitative purposes, absorbances at peak maxima at $\lambda = 523$ nm were considered [41]. The ABTS•+ aqueous-phase samples were analyzed by measuring UV-Vis spectra (Perkin Elmer, model Lambda 465) using a TrayCell cuvette (Hellma, dilution factor 5, light path 2 mm), where we followed the decrease and increase of ABTS•+ absorption bands at 415 and 340 nm, respectively [40].

A 10 mg/L solution of bisphenol A (BPA) was used to investigate the photocatalytic degradation of this model organic pollutant. The BPA oxidation runs were carried out in a 250 mL batch slurry reactor made of glass (Lenz Laborglas, model LF60) at a constant temperature of 25 °C (Julabo, model F25/ME) and atmospheric pressure with a catalyst concentration of 125 mg/L. The BPA/catalyst suspension was during the experiment stirred at 600 rpm and purged with air with a flow rate of 750 mL per minute. After 30 min of the dark period, the illumination with visible light (Philips, 150 W, λ_{max}=520 nm) was started. The collected liquid-phase samples were filtered through a 0.2 μm membrane filter and analyzed using an HPLC instrument (Shimadzu, model LC-40) operating in the isocratic mode. The column (100 × 4.6 mm BDS Hypersil C18 (2.4 μm)) was thermostated at 30 °C, and a mixture of methanol and ultrapure water (70%: 30%, v/v) was used as the mobile phase. The flow rate of the mobile phase was equal to 0.5 mL per minute.

3. Results

The color of the pure TNR is white, and that of Au/TiO_2 catalysts is purple (Fig. S1). The intensity of the purple depends on the size of Au NPs in the Au/TiO_2 catalysts and occurs in the presence of Au NPs between 20 and 40 nm in diameter [42]. We always used TNR as a carrier and the same gold precursor (HAuCl$_4$·xH$_2$O for preparation of Au/TiO_2 catalysts, while varying three parameters during the catalyst preparation procedure, i.e. solvent, time of stirring, and calcination temperature.

The results of UV-Vis DR measurements are illustrated in Fig. 1, where we can see in the spectra of the Au/TiO_2 catalysts that light absorption occurs in two regions: (i) in the UV-light region (below 400
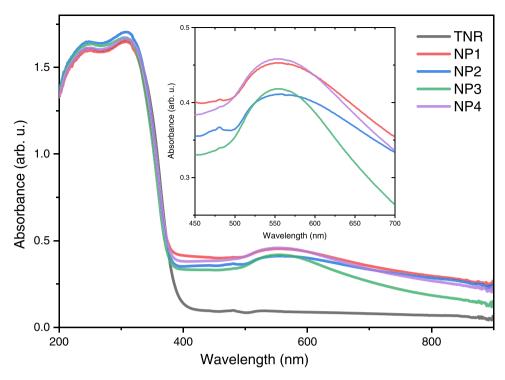
Fig. 1. UV-Vis DR spectra of the TNR support and catalysts containing 1.0 wt% of Au.

nm), which is due to the presence of TiO$_2$, and (ii) in the visible region between 450 and 600 nm, which is due to the presence of metallic Au nanoparticles in these solids and the LSPR effect originating from the plasmonic properties of Au. The obtained band gap energy of pure TNR is 3.2 eV, which is in good agreement with the literature data [8,9,11,12, 13]. The peak for Au NPs in Au/TiO$_2$ samples is single oval (inset in Fig. 1), which alludes that the obtained Au NPs are spherical [14]. This was further confirmed by the results of TEM analysis (presented below in Fig. 3). Finally, the presence of plasmonic effects in selected Au/TiO$_2$ catalysts under visible-light illumination was demonstrated by purposely designed experiments, which are described in the Supplementary Information.

The photoluminescence emissions are crucial for understanding the recombination rate of charge carriers (e^--h^+ pairs) in the examined Au/ TiO$_2$ catalysts. In heterogeneous photocatalysis for wastewater treatment, the recombination rate of charge carriers needs to be low because electrons and holes need to preferentially participate in redox processes on the catalyst surface, i.e. to produce ROS or directly degrade molecules of a pollutant. The results of the solid-state PL measurements are shown in Fig. 2. High PL intensity means a high charge carrier recombination rate. The semiconducting TiO$_2$ exhibits this disadvantage, and by adding a plasmonic metal, the recombination rate of charge carriers, in principle, becomes lower [13]. As shown in Fig. 2, the pure TiO$_2$ sample shows the highest PL intensity, which means that it has the highest recombination rate of charge carriers. The lowest PL intensity is expressed by the NP3 catalyst, followed by NP1, NP4, and NP2 samples. The peak at 3.17 eV in the PL spectra of the investigated samples is attributed to the anatase form of TiO$_2$ [43,44]. A blue shift was observed in the PL spectra of Au/TiO$_2$ catalysts in the range of 3.17 eV to 3.23–3.25 eV compared to the PL spectrum of TNR support. Such range shift occurred because the Au ensembles selectively suppress phonon-assisted indirect transitions in anatase TiO$_2$ [45,46]. The lowest indirect transition $\Gamma_{1b} \rightarrow X_{1a}$ is indicated by the peak at 2.9 eV [47]. The presence of shallow trap levels, oxygen vacancies, and defects in the TNR support was indicated by peaks at 2.34, 2.55, and 2.7 eV [47,48]. To conclude, the results of solid-state PL measurements suggest that the addition of Au nanoparticles to TNR prolongs the "lifetime" of charge
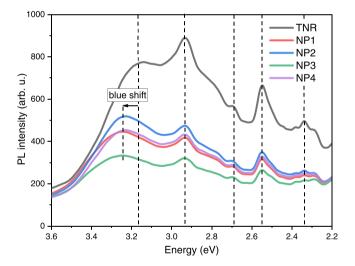

Fig. 2. Solid-state photoluminescence (PL) emission spectra of the investigated materials.

carriers due to the formation of a Schottky barrier (SB) between the TNR support and Au NPs, which acts as a sink for the visible-light generated "hot electrons" in Au. Furthermore, based on the results presented in Fig. 2, one can assume that among the investigated Au/TiO$_2$ catalysts, the NP3 sample would exhibit the highest photocatalytic activity in reactions in which superoxide anion radicals (O$_2^{\bullet-}$) are the predominant reactive oxygen species.

The results of SEM-EDXS analysis are listed in Table 1 and show that the actual Au loading in the synthesized Au/TiO$_2$ catalysts is close to the nominal loading of 1 wt%. Fig. S2 shows the arrangement of the elements Ti, O, and Au for obtained catalysts NP1, NP2, NP3, and NP4. All of them exhibit a homogeneous distribution of mapped elements, throughout the sample, with the expected higher proportions of Ti and O and a lower amount of gold.

The overview TEM micrographs of the Au/TiO$_2$ catalysts show a

Table 1
Results of SEM-EDXS analysis of the investigated TNR support and Au/TiO$_2$ catalysts.

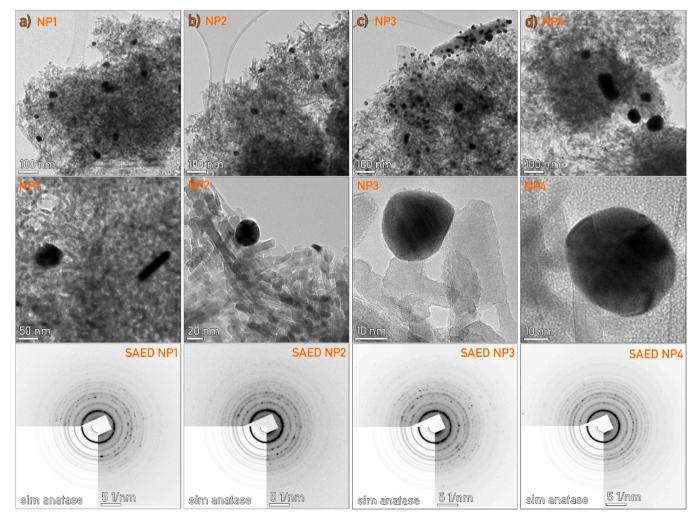| Sample		TNR	NP1	NP2	NP3	NP4
Ti	wt	54	53.5	52.6	52.7	54.3
	%	± 2.0	± 2.1	± 2.2	± 2.4	± 1.6
O		47	45.7	46.4	46.4	44.8
		± 2.0	± 2.1	± 2.3	± 2.3	± 1.6
Au		-	0.8 ± 0.1	1.0 ± 0.1	0.9 ± 0.1	0.9 ± 0.1

Analysis conditions: voltage 15 keV, ZAF correction method. The instrument was calibrated with an analytical mono-block from MAC.

uniform distribution of Au nanoparticles scattered over the TiO$_2$ support composed of anisotropic, rod-like anatase nanoparticles (Fig. 3). The TiO$_2$ particles in bare TNR were found to be 70 nm in length and 8 nm in width. The morphology of Au NPs is near-spherical, with only poorly developed Wulff shapes. At large magnification, we can see that many Au particles have internal structural defects, showing typical 5-fold twinning. Au NPs in the examined Au/TiO$_2$ solids were manually outlined on acquired TEM microscopic images and their size was calculated using the ImageJ program. The obtained particle size distribution histograms of Au NPs are shown in Fig. 4. One can see that the particle size distribution of Au NPs in the prepared NP1 and NP4 samples is broader, and several of the measured Au nanoparticles are larger than 100 nm. On the other hand, the Au particle size distribution in NP2 and NP3 samples is narrow, and the majority of obtained NPs exhibit a particle

size of about 20–30 nm. The average Au particle size in Au/TiO$_2$ catalysts is listed in Table 2. Au NPs tend to be of larger diameter, which was also observed by Verma et al. [35].

The results of the N$_2$ physisorption analysis are listed in Table 2 and illustrated in Fig. S3. They show that the specific surface area (S_{BET}), pore volume (V_{pore}), and pore diameter (d_{pore}) of the Au/TiO$_2$ catalysts are mainly dominated by the morphological properties of the TNR support, as they do not change significantly in comparison to the pure TNR support upon Au loading. The low extent of changes further indicates that the loading of 1.0 wt% Au on the catalyst surface does not block the pores of TNR support. Fig. S3a shows the classical adsorption-desorption N$_2$ isotherm of samples TNR, NP1, NP2, NP3, and NP4. All catalysts belong to the classification group of mesoporous materials, as we obtained classic type IV isotherm curves [49] for all catalysts. That kind of curve corresponds to materials with a pore size of 2–50 nm. Due to a typical shape of curves at $p/p_0 = 1$, one can conclude that the catalysts also contain pores larger than 50 nm, i.e. macropores [50]. Fig. S3b shows the derived pore size distribution for all catalysts. All of them exhibit a similar trend, and the pores are in the range between 10 and 20 nm. It follows that the addition of gold NPs has no significant effect on the pore size distribution.

The H$_2$-TPR technique was used to investigate metal-support interactions in Au/TiO$_2$ photocatalysts [51]. Fig. 5 shows that in the obtained H$_2$-TPR profiles, two regions can be distinguished (arbitrarily determined by deconvolution): (i) low-temperature region below 300 °C region, in which H$_2$ consumption can be attributed to the reduction of

Fig. 3. Overview TEM micrographs of Au/TiO$_2$ catalysts recorded at the same magnification. Selected regions are further magnified in the second row. Samples a) NP1, b) NP2, c) NP3, and d) NP4, with corresponding experimental SAED pattern, compared to simulated anatase diffraction (sim anatase).
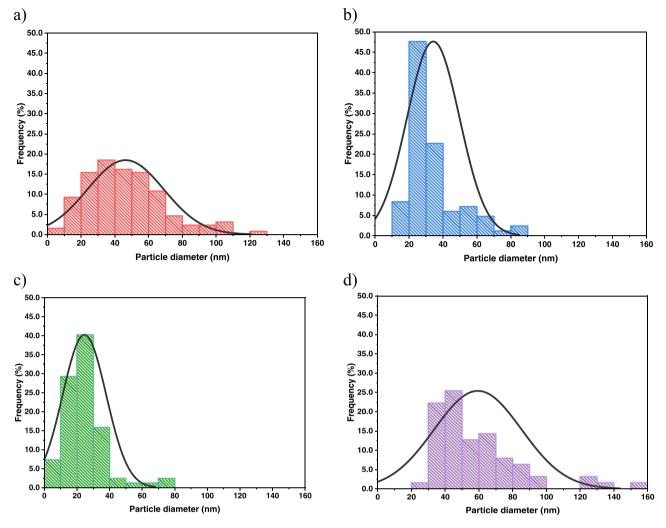
Fig. 4. Particle size distribution of Au ensembles over the TNR support in catalyst samples a) NP1, b) NP2, c) NP3, and d) NP4.

Table 2

Results of N_2 physisorption (specific surface area (S_{BET}), pore volume (V_{pore}), and pore diameter (d_{pore})), XRD (the apparent crystallite size of anatase and the crystallite size gold were calculated from the diffraction peaks at 25 and 44°, respectively, using the Scherrer equation), TEM (average size of Au NPs), EIS (comparison of charge transfer resistance (R_{CT})) and XPS (Schottky barrier height (SBH)) analyses of the investigated TNR support and Au/TiO$_2$ catalysts.

Sample	TNR	NP1	NP2	NP3	NP4
S_{BET} (m^2/g)	106	105	93.8	101	105
V_{pore} (cm^3/g)	0.48	0.47	0.44	0.45	0.47
d_{pore} (nm)	18.3	17.9	18.9	17.9	17.8
[a]Apparent anatase crystallite size (nm)	17.4	17.4	17.4	17.4	17.4
Au crystallite size (nm)	-	9.1	18.4	9.1	9.1
Average size of Au NPs (nm)	-	49.8	33.6	22.8	42.8
R_{CT} (kΩ)	1154	513	456	306	524
SBH (eV)	-	0.10	0.24	0.33	0.18

[a] The apparent values were calculated because the TNR support is non-spherical.

Fig. 5. H$_2$-TPR profiles of the TNR support and synthesized Au/TiO$_2$ catalysts.

TiO$_2$ support that occurs via dissociative adsorption of H$_2$ on the surface of Au ensembles and migration of H* species to the support (spillover effect), and (ii) high-temperature reduction of TiO$_2$ support by H$_2$ to produce TiO$_{2-x}$. The largest area under the H$_2$-TPR curves up to 300 °C was obtained in the case of sample NP3. This is because sample NP3 exhibits both the lowest average Au particle size and the largest number of small Au nanoparticles (Fig. 4, Table 2). The smaller the Au particles
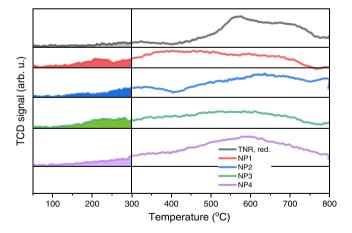
are, the stronger the interaction between TiO$_2$ and Au NPs. The areas under the H$_2$-TPR curves in the temperature range from 50 to 300 °C were smaller for the remaining Au/TiO$_2$ samples and in the following order: NP1 > NP2 > NP4, which is related to the abundance of very small Au aggregates on the TiO$_2$ surface (see Fig. 4). We can therefore conclude that the results of H$_2$-TPR analysis are in good agreement with the results of TEM analysis.
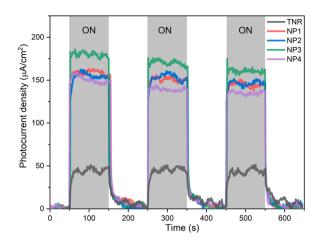
The results of the XRD analysis are shown in Fig. 6 and listed in Table 2. It is known that TiO$_2$ is found in nature in the three most common polymorphs: rutile, brookite, and anatase [52]. The latter form is the most active; therefore, the anatase form of TiO$_2$ is aimed at the synthesis of nanorods. The XRD patterns (Fig. 6) confirm the presence of anatase TiO$_2$ in the investigated samples. Since the peaks of anatase TiO$_2$ are the same for the TNR support and Au/TiO$_2$ samples, we can conclude that TiO$_2$ was stable during both gold deposition with wet impregnation and subsequent calcination steps. Peaks for Au particles (present in the metallic state) are also visible in all XRD diffractograms for Au/TiO$_2$ samples. The apparent crystallite size of anatase TiO$_2$ (please note that the TNR support is non-spherical) and the crystallite size of gold were calculated from the diffraction peaks at 25 and 44°, respectively, using the Scherrer equation [53]. The apparent crystallite size of anatase in the TNR support is 17.4 nm. The same apparent crystallite size of anatase was also found in the Au/TiO$_2$ samples. This shows that the TNR support was not affected by the Au deposition process.

There is no significant change in the gold crystallite size in the calcined Au-containing samples (NP1, NP3, NP4). The largest Au crystallite size was observed in the non-calcined NP2 sample, most likely due to the agglomeration of particles by the HAuCl$_4$ precursor.
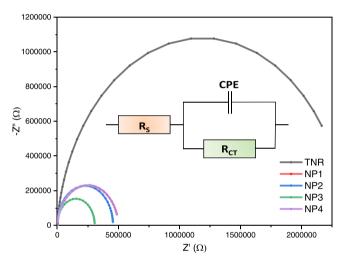
The results of the photocurrent density measurements are illustrated in Fig. 7. They show that the highest amount of the visible-light generated charge carriers was formed in the presence of the NP3 catalyst, while the lowest amount was observed over the NP4 sample. Samples NP1 and NP2 generated almost the same amount of visible-light-generated charge carriers. The ability of the investigated materials toward the separation of visible-light generated charge carriers was further tested using electrochemical impedance spectroscopy (EIS); the obtained results are illustrated in Fig. 8 in the form of Nyquist plots. The EIS measurements were fitted by the equivalent electrochemical circuit (EEC) shown in the inset of Fig. 8, which is composed of the solution resistance (R_S), charge transfer resistance (R_{CT}), and constant phase element (CPE). The R_{CT} values in the EEC listed in Table 2 indicate the value of charge transfer resistance at the electrode (photocatalyst)/ electrolyte interface since the diameter of the Nyquist diagram reflects the charge transfer process. R_{CT} is the ability to donate an electron to an electroactive species in a solution. The smaller the R_{CT}, the more easily the electron transfer can occur. A higher charge transfer resistance of a catalyst is expressed by a larger diameter of the semicircle and a higher R_{CT} value. The highest R_{CT} value was exhibited by the bare TNR support, while the R_{CT} values of the Au/TiO$_2$ catalysts were significantly smaller.

Survey spectra and high-resolution spectra for Ti 2p and Au 4 f are

Fig. 7. Off-on current density vs. time traces under visible-light illumination of the working electrode with deposited catalysts obtained in an aqueous solution of 0.1 M KOH.

Fig. 8. EIS Nyquist plot of bare TNR support and synthesized Au/TiO$_2$ catalysts in a 0.1 M KOH electrolyte under visible-light irradiation. The inset shows the electrochemical equivalent circuit used to fit the EIS measurements that include a solution resistance (R_S), charge transfer resistance (R_{CT}), and constant phase element (CPE).

given in Fig. 9. Survey spectra for NP samples show that they comprise O- (O 1 s signal), Ti- (Ti 2p, Ti 3 s, and Ti 3p signals), and C-containing (C 1 s signal) species (Fig. 9a). On the other hand, the Au 4 f signals representing Au are not intense in all survey spectra of the samples from NP. Ti 2p$_{3/2}$ peaks for all samples are located at 458.7 eV (Fig. 9b), indicating Ti(IV) [54]. Although the Au content was low, the Au 4 f spectra were still well-defined (Fig. 9c). The Au 4 f$_{7/2}$ peak was at 83.4 eV in all spectra, which is at more negative binding energies than the expected position of 84.0 eV for bulk Au. It has been previously reported that the peak shift to more negative binding energies may be due to electron transfer from the carrier to the nanoparticles [55]. However, the oxidation state of Au does not change for any of the tested NP samples, and it can be confirmed that Au is in the metallic state (Au was not oxidized).

The Schottky barrier (SB) is a barrier formed at the junction between the plasmonic metal (e.g., Au) and the semiconductor, and controls the transfer of hot charge carriers between the contacted metal and semiconductor [18,21,22]. The SBH ($\varnothing_{SB}$) is determined as [56,57]:

$$\varnothing_{SB} = \varnothing_M - \chi \tag{1}$$

Fig. 6. XRD diffractograms of the TNR support and catalysts containing 1.0 wt % of Au loading. Solid vertical lines belong to anatase TiO$_2$ (JCPDS 00–021–1272) and dotted vertical lines belong to Au (JCPDS 01–1174). Gold crystallite sizes were calculated from XRD data using the Scherrer equation and are listed in Table 2.
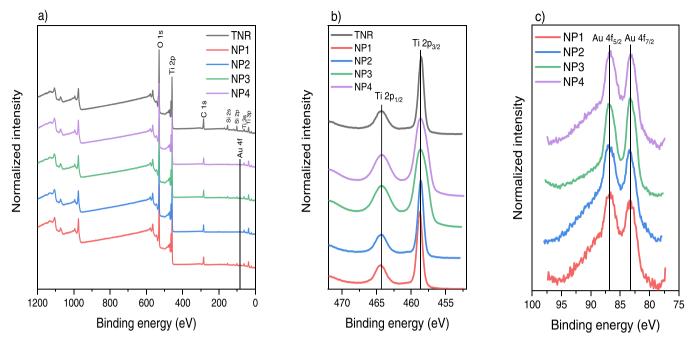
Fig. 9. a) Survey spectra for NP1, NP2, NP3, NP4, and TNR samples. High-resolution b) Ti 2p and c) Au 4 f spectra for NP1, NP2, NP3, and NP4 samples.

where $\varnothing_M$ represents the work function of Au and χ represents the electron affinity of the TNR support. The positions of the valence band maxima (VBM) for the investigated samples are shown in Fig. 10, and the calculated SBH values are listed in Table 2. The SBH values are in the range of 0.1–0.3 eV. The obtained SBH values agree with the results reported previously that SBH values are in the range of 0.1–1 eV [13,22, 58]. The obtained SBH values listed in Table 2 further show that in the present case, the height of SB increases with the decreased average size of Au ensembles. Moon et al. [59] studied the effect of Au NPs size on SBH and concluded that the larger the Au NPs are, the higher SBH is. On the other hand, Žerjav et al. [60] recently demonstrated that with the increase in the diameter of Au NPs, the SBH decreases. Marri et al. reported that the presence of oxygen defects influences the formation and height of the SB [58], which might contribute to differences in reports [59,60]. In principle, low SBH is desired during the transfer of "hot electrons" from the plasmonic metal to the TiO$_2$ support, as a high SBH can lead to the agglomeration of "hot electrons" at the SB. The agglomerated "hot electrons" can then more easily recombine with holes

generated in the plasmonic metal and are lost for generating ROS or directly degrading water-dissolved organic pollutants. However, it should be noted that the SB also presents a barrier to the electrons, which tend to be transferred from the TiO$_2$ support to plasmonic metal nanoparticles.

To monitor the ability of investigated samples to produce OH$^\bullet$ radicals (via H$_2$O$_2$ produced from superoxide anion radicals), photocatalytic oxidation of the aqueous solution of coumarin was carried out. Oxidation of coumarin with OH$^\bullet$ radicals results in the formation of 7-hydroxycoumarin (7-OHC) as a fluorescently active compound [17], the temporal concentration of which can be monitored by EPR [37,40, 61], luminescence [37,62,63] and UV-Vis fluorescence measurements [37,64]. The latter analytical technique was employed in this study, and the obtained results are illustrated in Fig. 11. It can be seen that the generation of 7-OHC was favored in the presence of NP1 and NP4 samples, containing the largest Au NPs on the catalyst surface. Considerably slower formation of 7-OHC was observed in the case of NP2 and
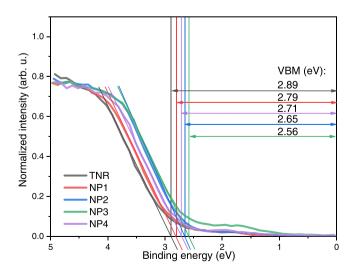

Fig. 10. Determination of VBM of pure TNR support and Au/TiO$_2$ catalysts using XPS analysis.
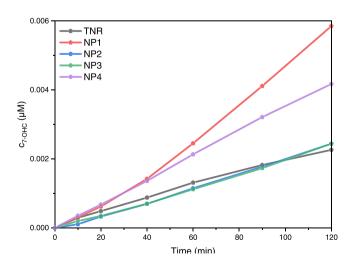

Fig. 11. Dependence of 7-hydroxycoumarin (7-OHC) concentration on irradiation time, measured upon visible-light illumination of aqueous suspensions containing investigated catalysts and coumarin (COUM).
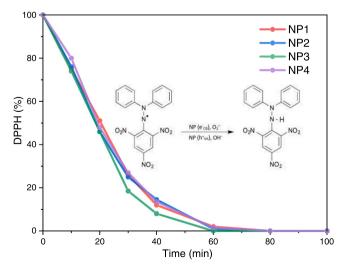
NP3 catalysts (smaller Au NPs on the catalyst surface). The photocatalytic activity regarding the formation of OH$^\bullet$ radicals decreases in the following order: NP1 > NP4 > > NP2 ≈NP3.

In the given range of operating and reaction conditions, from the EPR spectra displayed in Fig. S4, there was no visible signal for OH$^\bullet$ radicals (as a POBN-OH adduct) after 4 h of illumination of NP1 catalyst with the visible-light source. Compared to the UV-Vis fluorescence technique (Fig. 11), the signal-to-noise ratio was too low to identify trace amounts of OH$^\bullet$ radicals. After 4 h, we added 5 μL of H$_2$O$_2$ into the reaction suspension (which resulted in c(H$_2$O$_2$)= 0.98 μmol/L). The sample was collected after 3 min, and the signal for OH$^\bullet$ radicals (sextet of peaks belonging to the POBN-OH adduct) was evidenced in the acquired EPR spectrum. This confirms that the NP1 catalyst enables homolytic cleavage of H$_2$O$_2$ to produce OH$^\bullet$ radicals.
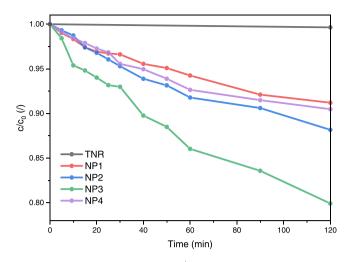
The photocatalytic measurements using DPPH, a semi-stable free radical that can accept electrons from reactive radicals and resembles the behavior of radical scavengers [40], reflect the formation of several species, i.e. e^-, O$_2^{\bullet-}$, h$^+$, and OH$^\bullet$. The DPPH relative concentration vs. irradiation time dependencies illustrated in Fig. 12 were obtained by monitoring the change of color of the reaction suspension from purple to yellow by measuring absorbance at 523 nm. As we can see, the DPPH disappearance rates are, within an experimental error, almost the same for all Au/TiO$_2$ catalysts. We believe this is a consequence of the readiness of DPPH to react with all the above-mentioned species produced on the surface of Au/TiO$_2$ catalysts.

Fig. 13 shows the relative concentration of 2,2′-azino-bis(3-ethyl-benzothiazoline-6-sulphonate) cation (ABTS$^{\bullet+}$) as a function of visible-light illumination time in the presence of bare TNR support and Au/TiO$_2$ samples to monitor the generation of e^- and formation of O$_2^{\bullet-}$. The highest ABTS$^{\bullet+}$ reduction rate was obtained in the NP3 sample. However, the other Au/TiO$_2$ samples exhibited lower ABTS$^{\bullet+}$ reduction rates. The photocatalytic activity regarding the generation of superoxide anion radicals (O$_2^{\bullet-}$) decreases in the following order: NP3 > > NP2 > NP4 > NP1, i.e. by increasing the average size of Au NPs or decreasing SBH (Table 2).
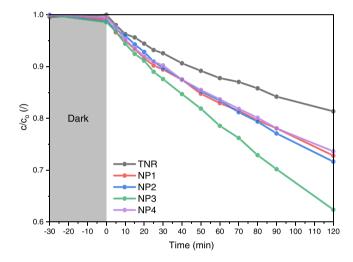
Fig. 14 shows the results of visible-light-triggered BPA degradation investigated in the presence of prepared Au/TiO$_2$ photocatalysts. BPA can be oxidized by both O$_2^{\bullet-}$ and OH$^\bullet$ radicals [65,66]. The results show that the sample NP3, exhibiting the lowest average diameter of Au NPs on the catalyst surface, enabled the highest BPA degradation rate. The samples NP1, NP2, and NP4 were less active and exhibited similar BPA degradation rates. After 120 min of reaction course, the sample NP3 enabled almost 40% of BPA disappearance, while for other Au/TiO$_2$ catalysts, BPA conversion was found to be close to 30%. The

Fig. 13. Relative concentration of ABTS$^{\bullet+}$ as a function of time obtained in the presence of investigated photocatalysts under visible-light illumination.

Fig. 14. Photocatalytic degradation of BPA dissolved in water (V=250 mL, c_0 =10.00 mg/L) under visible-light illumination obtained at T = 25 °C in the presence of pure TNR support and Au/TiO$_2$ catalysts (125 mg/L).

photocatalytic activity of the bare TNR support can be attributed to the presence of Ti^{3+} species on the surface or surface defects [67], which is also in agreement with the findings of solid-state PL analysis (Fig. 2). The results of our research work are in good correlation with the results of the research work of Kumar et al. [15] and Singh et al. [16], where the highest photocatalytic activity was exhibited by the Au/TiO$_2$ catalysts where anatase TiO$_2$ was used. Žerjav et al. [60] investigated TiO$_2$-based catalysts containing gold. The synthesized catalysts were used for the degradation of BPA (c_0 =10.0 mg/L, $m_{cat.}$=125 mg/L) under visible-light illumination. After 120 min of reaction time, the highest degradation (almost 70%) was observed for the catalyst with the highest gold loading (i.e. 2.0 wt%). Cojocaru et al. [68] also studied the degradation of BPA over Au/TiO$_2$ catalysts. The reaction was carried out under visible-light illumination in a reactor containing 10 mg of a catalyst and 66.8 mg/L of aqueous BPA solution. After 24 h of illumination, the degradation of BPA was 80%, for catalysts containing 0.3–0.7 wt% of gold. Roškarić et al. [69] added g-C$_3$N$_4$ to TiO$_2$ catalysts to increase the catalytic activity of pure TiO$_2$. After 2 h of reaction under visible-light illumination (c_0 =10 mg/L, $m_{cat.}$=125 mg/L), BPA degradation was 35%.

We can conclude that the observed photocatalytic activity of the investigated Au/TiO$_2$ catalysts for BPA removal (Fig. 14) is a

Fig. 12. Relative concentration of DPPH as a function of time obtained in the presence of investigated photocatalysts under visible-light illumination.

consequence of the different abilities of Au/TiO$_2$ catalysts for the generation of O$_2^{\bullet-}$ (Fig. 13) and OH$^\bullet$ radicals (Fig. 11). Nevertheless, the results show that BPA oxidation conducted in the presence of synthesized Au/TiO$_2$ catalysts is predominantly governed by superoxide anion radicals (O$_2^{\bullet-}$).

4. Discussion

Based on the results of the TEM analysis, we see that the Au NPs obtained on the TNR support are of different sizes. The Au NPs in sample NP2 are smaller than in sample NP1, which means that the gold NPs agglomerated during the thermal treatment at 300 °C and formed larger nanoparticles. The reason for this is that larger particles have a larger volume-to-surface area ratio, which is more energetically optimal [70]. The size of NPs in sample NP3 is smaller than in sample NP1, probably due to the longer stirring time during the catalyst preparation procedure. In sample NP4 (dispersed in water), we obtained larger NPs than in sample NP1 (dispersed in ethanol). From the results of the TEM analysis (Figs. 3 and 4), we can conclude that the best way to obtain smaller NPs is to disperse them in ethanol and stir them for a longer time.

A comparison of the dependencies depicted in Figs. 13 and 14 shows that superoxide anion radicals (O$_2^{\bullet-}$) represent the main reactive oxygen species that determine the priority oxidation pathway and the decay of BPA as a model organic pollutant on the surface of the studied Au/TiO$_2$ catalysts. Concerning the formation of OH$^\bullet$ radicals, the size of Au NPs is the main reason for the obtained results of the COUM test reaction illustrated in Fig. 11. At a first glance, these results are in contrast to the observations of the solid-state PL measurements (Fig. 2), tests employing other radical scavengers (Figs. 12 and 13), and experiments of photocatalytic BPA oxidation (Fig. 14), according to which sample NP3 should exhibit the fastest formation of hydroxyl radicals. However, it should be pointed out that OH$^\bullet$ radicals, the formation of which is monitored by the COUM test reaction, are produced by the homolytic cleavage of H$_2$O$_2$ (Fig. S4), which was previously formed by reactions involving superoxide anion radicals (O$_2^{\bullet-}$). One should note that under visible-light illumination of Au/TiO$_2$, OH$^\bullet$ radicals cannot be formed via the participation of VB holes in the TNR support. The degradation of H$_2$O$_2$ takes place on the surface of Au NPs and is faster in the presence of larger Au NPs (NP1 catalyst) because the latter exhibit more metallic character than smaller Au NPs (NP3 catalyst). Consequently, the fastest formation of OH$^\bullet$ radicals was observed in the presence of NP1 catalyst, which exhibits the largest average Au particle size among the Au/TiO$_2$ solids tested (Table 2).

Formation of "hot electrons" and superoxide anion radicals (O$_2^{\bullet-}$) was favored in the presence of the NP3 sample (Fig. 13). This catalyst exhibits the highest SBH and the smallest average particle size of Au NPs among the investigated Au/TiO$_2$ composites (Table 2). The opposite was found for the NP1 catalyst. Low SBH would be advantageous to facilitate the transfer of "hot electrons" from the plasmonic metal to the TiO$_2$ support in cases when they could easily migrate and take place in subsequent surface reactions, e.g. O$_2$ reduction. When there exists no "sink" for "hot electrons" already transferred from the plasmonic metal to the TiO$_2$ support (i.e. O$_2$ reduction is slow), then, on the contrary, the presence of high Schottky barrier would be advantageous to prevent the transfer of electrons from the CB of TiO$_2$ support to plasmonic metal nanoparticles. Obviously, in the present work, it was the latter scenario. These findings differ from our previous work [60], where the rate of BPA degradation increases with decreasing SBH, while the results presented in Figs. 13 and 14 show that the photocatalytic activity for ABTS$^{\bullet+}$ reduction and BPA oxidation increase with increasing SBH. In the present work, Au nanoparticles were deposited on TiO$_2$ in the form of nanorods, while in the previous work, commercially available TiO$_2$ nanoparticles were used as a carrier. Since the Au nanoparticles in both works are of comparable size, the differences in the photocatalytic behavior of the Au/TiO$_2$ catalysts might be attributed to different surface properties. This will be the subject of further research.

5. Conclusions

The Au/TiO$_2$ plasmonic catalysts were synthesized using the wet impregnation technique and different media (water or ethanol), stirring times, and calcination. The UV-Vis DR spectra of the investigated materials show light absorption of TiO$_2$ in the UV range and light absorption of metallic Au nanoparticles in the visible range due to the LSPR effect. The results of solid-state PL measurements reveal that the lowest PL intensity and the lowest charge carrier recombination rate were expressed by the NP3 sample exhibiting the highest Schottky barrier. SEM-EDXS and TEM analyses show that all synthesized samples are loaded with 1 wt% Au and that the obtained Au nanoparticles are nanosized. BET surface area, pore volume, and pore size decrease upon calcination of the Au/TiO$_2$ materials. The alteration in the values is low, except for the sample NP2. This indicates that the deposited Au ensembles did not block the pores of TiO$_2$ nanorods.

From the results of reactive oxygen species formation, we could confirm that the examined Au/TiO$_2$ catalysts generate charge carriers, i. e. superoxide anion (O$_2^{\bullet-}$) and OH$^\bullet$ radicals, under visible-light illumination. Based on the results of photocatalytic BPA degradation, we can conclude that increasing the stirring time during the catalyst preparation procedure resulted in the formation of an Au/TiO$_2$ catalyst that enables higher charge carrier generation and BPA conversion rates. Superoxide anion radicals (O$_2^{\bullet-}$) represent the main reactive oxygen species that determine the priority oxidation pathway and the decay of BPA as a model organic pollutant on the surface of the studied Au/TiO$_2$ catalysts. The activity of the latter for the generation of O$_2^{\bullet-}$ radicals and BPA oxidation increases by increasing the Schottky barrier height and decreasing the average size of Au ensembles on the surface of TiO$_2$ nanorods.

CRediT authorship contribution statement

Špela Slapničar: Investigation, Methodology, Visualization, Writing - Original Draft, Writing - Review & Editing, Gregor Žerjav: Investigation, Visualization, Writing - Review & Editing, Janez Zavašnik: Investigation, Visualization, Writing - Review & Editing, Matjaž Finšgar: Funding acquisition, Investigation, Visualization, Writing - Review & Editing, Albin Pintar: Funding acquisition, Project administration, Conceptualization, Supervision, Writing - Review & Editing.

Declaration of Competing Interest

The authors declare that they have no known competing financial interests or personal relationships that could have appeared to influence the work reported in this paper.

Data Availability

Data will be made available on request.

Appendix A. Supporting information

Supplementary data associated with this article can be found in the online version at doi:10.1016/j.jece.2023.109835.

References

1 V. Loddo, M. Bellardita, G. Camera-Roda, F. Parrino, L. Palmisano, Curr. Trends Futur. Dev. Membr. (2018) 1–43.

2 A. Tanaka, K. Hashimoto, H. Kominami, Chem. Commun. 53 (2017) 4759–4762.

3 J. Schneider, M. Matsuoka, M. Takeuchi, J. Zhang, Y. Horiuchi, M. Anpo, D. W. Bahnemann, Chem. Rev. 114 (2014) 9919–9986.

4 S. Foteinis, E. Chatzisymeon, Nanostruc. Photo (2020) 75–97.

5 M.I. Litter, Appl. Catal. B 29 (1999) 89–114.

6 M.R. Hoffmann, S.T. Martin, W. Choi, D.W. Bahnemann, Chem. Rev. 95 (1995) 69–96.

7 F. Hamidi, F. Aslani, Nanomat 9 (2019) 1444.

8 A. Fujishima, T.N. Rao, D.A. Tryk, J. Photochem. Photobiol. C. 1 (2000) 1–21.

9 M. Pelaez, N.T. Nolan, S.C. Pillai, M.K. Seery, P. Falaras, A.G. Kontos, P.S.M. Dunlop, J.W.J. Hamilton, J.A. Byrn, K. OShea, M.H. Entezari, D.D. Dionysiou, Appl. Catal. B 125 (2012) 331–349.

10 R. Andreozzi, V. Caprio, A. Insola, R. Marotta, Catal. Today 53 (1999) 51–59.

11 C. Dette, M.A. Pérez-Osorio, C.S. Kley, P. Punke, C.E. Patrick, P. Jacobson, F. Giustino, S. Jung, K. Kern, Nano Lett. 14 (2014) 6533–6538.

12 D. Bahnemann, D. Bochelmann, R. Goslich, Sol. Energy Mater. 24 (1991) 564–583.

13 G. Žerjav, J. Zavašnik, J. Kovač, A. Pintar, Appl. Surf. Sci. 543 (2021), 148799.

14 J. Zhang, X. Suo, J. Zhang, B. Han, P. Li, Y. Xue, H. Shi, Mat. Lett. 162 (2016) 235–237.

15 A. Kumar, P. Choudhary, V. Krishnan, Appl. Surf. Sci. 578 (2022), 151953.

16 J. Singh, K. Sahu, B. Satpati, J. Shah, R.K. Kotnala, S. Mohapatra, J. Phys. Chem. Solids 135 (2019), 109100.

17 G. Žerjav, A. Albreht, I. Volk, A. Pintar, Appl. Catal. A 598 (2021), 117566.

18 M.R. Khan, T.W. Chuan, A. Yousuf, M.N.K. Chowdhury, C.K. Cheng, Catal. Sci. Tehnol. 5 (2015) 2522–2531.

19 B.Y. Zheng, H. Zhao, A. Manjavacas, M. McClain, P. Nordlander, N.J. Halas, Nat. Commun. 6 (2015) 7797.

20 C. Clavero, Nat. Photonics 8 (2014) 95–103.

21 Z. Sun, Y. Fang, Sci. Rep. 11 (2021).

22 M.S. Arshad, Š. Trafela, K. Žužek Rožman, J. Kovač, P. Djinović, A. Pintar, J. Mater. Chem. 5 (2017) 10509–10516.

23 L.G. Devi, R. Kavitha, Appl. Surf. Sci. 360 (2016) 601–622.

24 D.T. Thompson, Nanotoday 2 (2007) 40–43.

25 S.D. Brown, P. Nativo, J.-A. Smith, D. Stirling, P.R. Edwards, B. Venugopal, D.J. Flint, J.A. Plumb, D. Graham, N.J. Wheate, J. Am. Chem. Soc. 132 (2010) 4678–4684.

26 G. Peng, U. Tisch, O. Adams, M. Hakim, N. Shehada, Y.Y. Broza, S. Billan, R. Abdah-Bortnyak, A. Kuten, H. Haick, Nat. Nanotech 4 (2009) 669–673.

27 M.E. Ali, S. Mustafa, U. Hashim, Y.B. Che Man, K.L. Foo, J. Nanomat (2012).

28 R. Amrollahi, M.S. Hamdy, G. Mul, J. Catal. 319 (2014) 194–199.

29 A. Ayati, A. Ahmadpour, F.F. Bamoharram, B. Tanhaei, M. Mänttäri, M. Sillanpää, Chemosphere 107 (2014) 163–174.

30 M. Luna, J.M. Gatica, H. Vidal, M.J. Mosquera, Chem. Eng. J. 368 (2019) 417–427.

31 D. Tsukamoto, Y. Shiraishi, Y. Sugano, S. Ichikawa, S. Tanaka, T. Hirai, J. Am. Chem. Soc. 134 (2012) 6309–6315.

32 M. Haruta, M. Date, Appl. Catal. A 222 (2001) 427–437.

33 S.M. Yoo, S.B. Rawal, J.E. Lee, J. Kim, H.-Y. Ryu, D.-W. Park, W.I. Lee, Appl. Catal. A 499 (2015) 47–54.

34 G. Žerjav, M.S. Arshad, P. Djinović, J. Zavašnik, A. Pintar, Appl. Catal. B 209 (2017) 273–284.

35 P. Verma, K. Mori, Y. Kuwahara, S. June Cho, H. Yamashita, Catal. Today 352 (2020) 255–261.

36 M. Kowalkińska, P. Głuchowski, T. Swebocki, T. Ossowski, A. Ostrowski, W. Bednarski, J. Karczewski, A. Zielińska-Jurek, J. Phys. Chem. C. 125 (2021) 25497–25513.

37 G. Louit, S. Foley, J. Cabillic, H. Coffigny, F. Taran, A. Valleix, J.P. Renault, S. Pin, Rad, Phys. Chem. 72 (2005) 119–124.

38 E.N. Hristea, M. Hillebrand, M.T. Caproiu, H. Caldararu, T. Constantinescu, A. T. Balaban, Arkivoc (2002) 123–132.

39 M.C. Foti, J. Agric. Food Chem. 63 (2015) 8765–8776.

40 V. Brezová, D. Dvoranová, A. Staško, Res. Chem. Intermed. 33 (2007) 251–268.

41 R. Isono, T. Yoshimura, K. Esumi, J. Colloid Interface Sci. 288 (2005) 177–183.

42 A.K. Vala, Synth React, Inorganic, Met. -Org., Nano-Met. Chem. 44 (2014) 1243–1246.

43 V. Jovic, Z.H.N. Al-Azri, W.T. Chen, D. Sun-Waterhouse, H. Idriss, G.I.N. Waterhouse, Top. Catal. 56 (2013) 1139–1151.

44 N. Serpone, D. Lawless, R. Khairutdinov, J. Phys. Chem. 99 (1995) 16646–16654.

45 H. Nakajima, T. Mori, M. Watanabe, J. Appl. Phys. 96 (2004) 925–927.

46 H. Nakajima, T. Mori, Phys. B 376–377 (2006) 820–822.

47 N.D. Abazović, M.I. Čomor, M.D. Dramićanin, D.J. Jovanović, S.P. Ahrenkiel, J. M. Nedeljković, J. Phys. Chem. B 110 (2006) 25366–25370.

48 Z.H.N. Al-Azri, W.T. Chen, A. Chan, V. Jovic, T. Ina, H. Idriss, G.I.N. Waterhouse, Top. Catal. 56 (2013) 1139–1151.

49 F.J. Sotomayor, K.A. Cychosz, M. Thommes, Acc. Mater. Surf. Res. 3 (2018) 34–50.

50 P. Bertier, K. Schweinar, H. Stanjek, A. Ghanizadeh, C.R. Clarkson, A. Busch, N. Kampman, D. Prinz, A. Amann-Hildenbrand, B.M. Krooss, V. Pipich, C.M. S. Workshop, Lectures 21 (2016) 151–161.

51 M.Y. Byun, Y.E. Kim, J.H. Baek, J. Jae, M.S. Lee, RSC Adv. 12 (2022) 860–868.

52 G. Žerjav, K. Žižek, J. Zavašnik, A. Pintar, J. Environ. Chem. Eng. 10 (2022), 107722.

53 W.-T. Chen, A. Chan, Z.H.N. Al-Azri, A.G. Dosado, M.A. Nadeem, D. Sun-Waterhouse, H. Idriss, G.I.N. Waterhouse, J. Catal 329 (2015) 499–513.

54 M.C. Biesinger, L.W.M. Lau, A.R. Gerson, R.St.C. Smart, Appl. Surf. Sci. 257 (2010) 887–898.

55 M. Sankar, Q. He, M. Morad, J. Pritchard, S.J. Freakley, J.K. Edwards, S.H. Taylor, D. J. Morgan, A.F. Carley, D.W. Knight, C.J. Kiely, G.J. Hutchings, A.C.S. Nano 6 (8) (2012) 6600–6613.

56 Z. Zhang, J.T. Yates, Chem. Rev. 112 (2012) 5520–5551.

57 R.T. Tung, Appl Phys, Rev 1 (2014), 011304.

58 I. Marri, S. Ossicini, Solid State Commun. 147 (2008) 205–207.

59 S.Y. Moon, H.C. Song, E.H. Gwag, I.I. Nedrygailov, C. Lee, J.J. Kim, W.H. Doh, J. Y. Park, Nanoscale 10 (2018) 22180–22188.

60 G. Žerjav, M. Roškarič, J. Zavašnik, J. Kovač, A. Pintar, Appl. Surf. Sci. 579 (2022), 152196.

61 Z. Barbieriková, D. Dvoranová, M.V. Sofianou, C. Trapalis, V. Brezová, J. Catal. 331 (2015) 39–48.

62 Y. Nosaka, A.Y. Nosaka, Chem. Rev. 117 (2017) 11302–11336.

63 K.-I. Ishibashi, A. Fujishima, T. Watanabe, K. Hashimoto, Electrochem. Commun. 2 (2000) 207–210.

64 O.I. Aruoma, Methods Enzymol. 233 (1994) 57–66.

65 P.V.L. Reddy, K.-H. Kim, B. Kavitha, V. Kumar, N. Raza, S. Kalagara, J. Environ. Manag. 213 (2018) 189–205.

66 Y.H. Tan, P.S. Goh, A.F. Ismail, Int. Biodeterior. Biodegrad. 102 (2015) 346–352.

67 M. Liu, X. Qiu, M. Miyauchi, K. Hashimoto, Chem. Mater. 23 (2011) 5282–5286.

68 B. Cojocaru, V. Andrei, M. Tudorache, F. Lin, C. Cadigan, R. Richards, V. I. Parvulescu, Catal. Today 284 (2017) 153–159.

69 M. Roškarič, G. Žerjav, J. Zavašnik, A. Pintar, J. Environ. Chem. Eng. 10 (2022), 107656.

70 A. Gołąbiewska, A. Malankowska, M. Jarek, W. Lisowski, G. Nowaczyk, S. Jurga, A. Zaleska-Medynska, Appl. Catal. B 196 (2016) 27–40, 2/15/2023; 3/28/2023; 3/ 30/2023.